APL Engineering Physics

RESEARCH ARTICLE | JULY 01 2026

Bound state in the continuum induced narrow resonances in MXene-coated absorptive dielectric metasurfaces for methane sensing

Shubhanshi Sharma ; Monica Pradhan ; Aviad Katiyi ; Alina Karabchevsky ;
Shailendra Kumar Varshney

APL Engineering Physics 1, 036101 (2026)
https://doi.org/10.1063/5.0332754

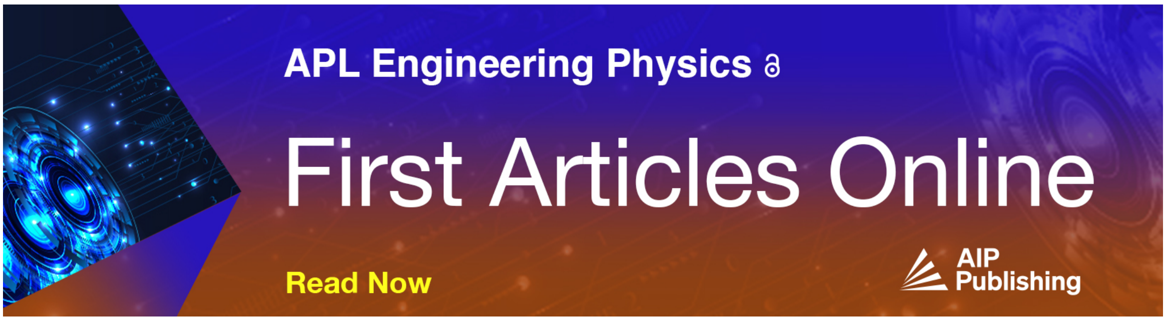

APL Engineering Physics ARTICLE pubs.aip.org/aip/aep

Bound state in the continuum induced narrow resonances in MXene-coated absorptive dielectric metasurfaces for methane sensing

Cite as: APL Eng. Phys. 1, 036101 (2026); doi: 10.1063/5.0332754
Submitted: 6 March 2026 • Accepted: 1 June 2026 •
Published Online: 1 July 2026

View Online Export Citation CrossMark

Shubhanshi Sharma,[1,a)] Monica Pradhan,[2] Aviad Katiyi,[3] Alina Karabchevsky,[3,4] and Shailendra Kumar Varshney[1]

AFFILIATIONS

[1] Department of Electronics and Electrical Communication Engineering, Indian Institute of Technology Kharagpur, Kharagpur, West Bengal 721302, India
[2] School of Nanoscience and Technology, Indian Institute of Technology Kharagpur, Kharagpur, West Bengal 721302, India
[3] School of Electrical and Computer Engineering, Ben-Gurion University of the Negev, Beer-Sheva 8410501, Israel
[4] Department of Physics, Lancaster University, Lancaster LA1 4YB, United Kingdom

[a)] Author to whom correspondence should be addressed: shubhanshi07@iitkgp.ac.in

ABSTRACT

Strong light confinement is essential for a range of applications, including sensing. MXene, a novel and emerging material with a broadband plasmonic response, active tunability, versatile surface chemistry with high adsorption efficiency, and flexibility, has been widely used in electronic sensing systems and has garnered significant attention for its applicability in photonics. The loss imparted by MXene can be overcome through the Bound States in Continuum (BIC) physics. In this work, we report two important designs of a hybrid metasurface, comprising a Silicon nanodisk metasurface and MXene. In both designs, a narrow and high absorption resonance of quality factor of ~150 is attained, where magnetic dipole is the dominant multipole, governed by symmetry-protected BIC. Both hybrid metasurface designs are optimized to exhibit a narrow resonance near 1650 nm with an absorption greater than 90%. The origin of high absorbance in such a hybrid metasurface is attributed to the momentum matching by SiO_2 spacer layer. The spectral characteristics of the designed metasurface can be used for first-overtone spectroscopy of methane gas. Numerical simulations yield a bulk refractive index sensitivity of 171 nm/RIU with FOM = 17.56 RIU^{-1} and sensitivity for methane gas, S = 0.8 nm per unit percentage concentration, when a Cryptophane-E layer is used. The designed sensor can also be tuned by varying the voltage across the MXene layer.

I. INTRODUCTION

Over the past few decades, artificially engineered structures known as metamaterials have attracted attention for their unique ability to manipulate electromagnetic wave amplitude and phase fronts.[1] The two-dimensional variants are referred to as metasurfaces, where individual elements (meta-atoms) couple resonantly with electric or magnetic or both components of the incident field and exhibit a response not found in nature.[2] With these versatile properties, metasurfaces demonstrate advantages in various applications such as *meta*-lensing,[3] cloaking,[4] holography,[5] sensing,[6] beam steering,[7] high-harmonic generation,[8] absorbers,[9] etc. Highly efficient and nearly perfect absorbers are widely applied in sensing, energy harvesting,[10] scattering reduction, modulation,[11] IR camouflage, and wireless communication. In optical sensing, light absorption is preferred, as it suppresses reflection and transmission, allowing energy to dissipate within the absorbing layer. The localized surface plasmon resonance (LSPR)[12] has been employed to create a resonant or a broadband absorber in plasmonic metasurfaces.[13,14] Alternatively, an all-dielectric metasurface supports two Mie resonances (electric and magnetic) whose overlap results in super and suppressed optical absorption.[15] Therefore, it is possible to achieve absorption of both electric and magnetic fields by suitable design and proper material selection.[16] The interference between multipoles results in non-radiating states,[17,18] one of which is the bound states in the continuum (BICs) that possesses an infinite lifetime. The BICs are the states confined within the continuum and remain decoupled from it.[19,20] These states ideally possess an infinite quality (Q) factor and cannot be observed in transmittance or reflectance spectra. The BIC, being a wave phenomenon, has been observed in photonics, phononics, and solid[19] systems. In photonics, it is observed for all the material systems (metal, dielectric, and hybrid).[21–24] BICs are of two types: one is governed by the system's symmetry, known as symmetry-protected BIC (SPBIC),[25] and the other arises due to the destructive interference of the states, known as accidental BICs.[26,27] Perturbations in geometry are generally introduced to observe the BICs in the spectra, transforming the non-radiative BICs into radiative quasi-BICs with a finite but high Q-factor exhibiting either Fano resonance or electromagnetically induced transparency (EIT).[28,29] Various fabrication approaches have been proposed in the existing literature to achieve the ultrahigh-Q BIC metasurfaces.[30–32]

In the context of symmetry-protected BIC, an ideal BIC becomes observable and converts into a quasi-BIC when the symmetry of the geometry is broken; such BICs have been observed in various geometries such as gratings, nanodisk, air channel embedded nanocube, and split ring nanoresonator, and many more.

Utilizing various physical mechanisms, different types of absorbers have been developed, including plasmonic absorbers governed by localized surface plasmon resonances (SPR), all-dielectric absorbers based on Mie resonances or BICs, and hybrid absorbers. The hybrid absorbers consist of metal and dielectric, which can yield near-unity absorption. Within this context, metals such as gold, silver, copper, and tungsten are widely used to make tunable devices that operate in different frequency bands.[43] Such structures work when surface plasmon resonance or localized surface plasmon resonance is hybridized with photonic Mie resonances, giving rise to plasmonic-photonics modes. Plasmons effectively manipulate light at the sub-diffraction scale, making them valuable for controlling light–matter interactions. Each resonance can absorb the incident energy by achieving a critical coupling state, where the radiative loss rate is the same as the material loss.[44] Hybrid multilayer structure-based broadband absorbers are designed in a way that works in visible[45] and mid-infrared[46] wavelength ranges. Besides these, metasurface absorbers have also been explored in the gigahertz (GHz),[47] terahertz (THz),[48] and ultraviolet (UV)[49] regions.

Despite promising capabilities, several limitations are associated with the use of metal in such devices. These include oxidation, melting, significant intrinsic losses, and high preparation costs. Metals such as gold are chemically inert, requiring complex surface functionalization for sensing applications, which has led to the exploration of alternative two-dimensional transition-metal materials, such as MXenes.

MXenes belong to the family of metal carbides, nitrides, and carbo-nitrides represented by the general formula $M_{n+1}X_nT_x$, where M refers to an early transition metal, X is either carbon or nitrogen, and T stands for surface functional groups, usually O, OH, or F.[50] These materials were initially discovered in 2011 at Drexel University by selectively removing the A layer (A-group mostly the elements of group 13 and 14)[51] from bulk ternary transition metal carbides and nitrides, known as MAX phases, resulting in the formation of multilayered MXenes.[52] MXenes exhibit high metallic conductivity, optical nonlinearity, and photothermal effect, due to the free electrons in their transition metal carbide or nitride backbone that contribute to their unique electronic structure.[53] The hydrophilic nature of MXene permits easy deposition on a wide range of substrates. Its anisotropic behavior leads to optical absorption spanning a broad bandwidth from the visible to the mid-infrared regions. It is considered an excellent candidate for efficient light absorption due to its stability and tunable surface chemistry.[54] It can also be tuned by varying the gate voltage or pump power.[55,56] They can be made photosensitive for flexible photodetector applications.[57] MXene possesses a direct bandgap that can be altered by varying the number of layers or modifying surface functional groups.[58] The surface functional groups of MXenes facilitate adsorption, while their large surface area enhances sensor sensitivity.[59,60] The aforementioned properties enable MXene to function as high-performance gas sensors at room temperature.[61] Recently, MXene has been used in optical fiber structures[62–65] to explore various sensing capabilities. MXene has also been explored in nanoscale platforms, such as metasurfaces composed of nanodisk, nanobars, and a multilayer of MXene/SiO_2, to achieve broadband absorption.[66–68]

In contrast to these broadband designs, the present work focuses on achieving a narrowband resonance response in the near-infrared region by utilizing MXene in conjunction with high-refractive-contrast materials, such as silicon (Si), and leveraging the physics of bound states in the continuum. The integration of Si metasurface driven by BIC resonances with MXene's plasmonic properties is anticipated to enable highly selective and efficient light–matter interactions, thereby paving the way for the development of next-generation, tunable, flexible, high-performance sensing platforms.

In this work, two design configurations are investigated in-depth to achieve high absorption over a narrow spectral range. In the first design, MXene is used as a thin film sandwiched between the dielectric spacer layer and the substrate, whereas the second design features a composite nanodisk. Both designs are composed of three materials: MXene, silica (SiO_2) spacer, and Si. These designs exhibit ultrahigh absorption, which is attributed to the physics of BIC in dielectric nanostuctures combined with the plasmonic response of MXene. Both configurations differ yet share nearly identical geometric parameters, resulting in a similar narrowband optical response. These designs, when integrated with the Cryptophane-E, a compound known for its selectivity for alkane, can be used for methane sensing with high sensitivity.

Here, Table I presents a comparison between the present work and previously reported works in the near-infrared and THz region, highlighting the novelty and advantages of our proposed MXene-based absorber design over previously reported works.[33–42] It is observed that most MXene-based sensors are reported in the THz region, exhibiting a broadband response, which contrasts with the present work, where the novelty lies in narrowband absorption with sensor application in the near-infrared region. The present work's Q-factor, sensitivity (S), and figure of merit (FOM) are comparable to those reported in existing works. Hence, the present work is of significant importance both for its novelty and simplicity, as it utilizes fewer materials to achieve a narrowband response.

TABLE I. Comparison of absorbers and related photonic sensing platforms. The table highlights differences in types of metasurfaces and materials used in the optical regime. In contrast to conventional metal losses, this work reports the integration of MXene with an all-dielectric BIC-supporting metasurface, enabling controlled dissipation channel.

Reference	Structures	Type	Materials	Q-factor	Absorptivity (%)	S	FOM (1/RIU)
33 (NIR)	Si nanodisk	BIC	$Si/SiO_2/Al$	1784	100	53.4 nm/RIU	63.1
34 (NIR)	Si nanoblocks	BIC	$Gr/Si/SiO_2/Ag$	170 000	100	108 nm/RIU	12 013
35 (NIR)	Compound grating	LSPR	$Au/SiO_2/Au/Si$	⋯	>93	⋯	28.7
36 (NIR)	Nanodisk with undercut	LSPR	$Al/SiO_2/Si$	⋯	⋯	245 nm/RIU	⋯
37 (NIR)	Quad nanodisks	BIC	$Si_3N_4/Au/SiO_2$	~100	⋯	306.4 nm/RIU	29.3
38 (THz)	Square and circular ring	LSPR	$Gr/MXene/SiO_2/Au$	750	99	4.2 THz/RIU	700
39 (THz)	Circular rings	LSPR	$Gr/MXene/SiO_2/Au$	47	99	0.214 THz/RIU	2.74
40 (THz)	Circular ring	⋯	MXene/polyimide	6.51	99.93	1.79 THz/RIU	1.91
41 (THz)	Circular ring	⋯	$MXene/Gr/SiO_2$	9.226	99.93	500 GHz/RIU	3.759
42 (THz)	Disk and crossbars	⋯	MXene/black phosphorus/Gr/SiO_2	35.822	≈68	1000 GHz/RIU	22.222
This work (NIR)	Si hollow nanodisk	BIC	$Si/MXene/SiO_2$	129	95	171 nm/RIU or 17.9 THz/RIU	17.5
This work (NIR)	Si hollow nanodisk	BIC	$MXene/SiO_2/Si/SiO_2$	184	85	⋯	⋯

II. METASURFACE DESIGNS AND WORKING PRINCIPLE

Figure 1 shows the 3D schematic of both hybrid metasurface designs and the top view of the unit cell with geometrical parameters. The design 1 metasurface comprises Si nanodisk resonators, where individual nanoresonators have a thorough air-hole channel offset from the nanodisk's center. The dielectric spacer of a thickness (t_{SiO_2}) is sandwiched between the metasurface and MXene thin film (t_{mx}). The whole structure is placed on a SiO_2 substrate, as depicted in Fig. 1(a). In the second design configuration (design 2), the composite nanodisk made up of MXene, a dielectric spacer, and Si (viewed from top to bottom) is placed over the silica substrate, as shown in Fig. 1(b). The composite nanodisk in design 2 also has an offset air channel. The design parameters have been optimized so that both metasurface designs yield high absorption. Note that for the optimization, we did not employ any algorithm; instead, we used a trial-and-error approach. The geometrical parameters in both designs are periodicity (Λ) = 865 nm, Si nanodisk of radius (r_{out}) = 268 nm, and air hole radius (r_{in}) = 80 nm. The Si nanodisk has a thickness of (t_{Si}) = 242 nm. However, the spacer thickness differs slightly between the two designs: t_{SiO_2} = 200 nm in design 1

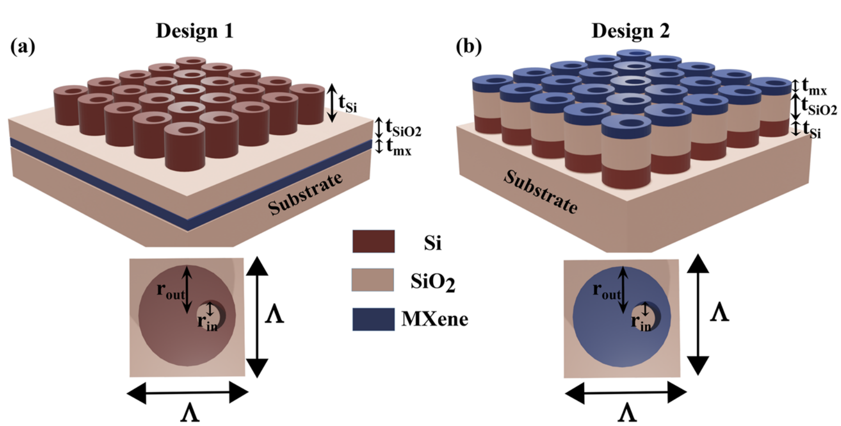

FIG. 1. 3D schematics of hybrid metasurface absorber with MXene in two design configurations, while the top view of a meta-atom is also shown at the bottom of individual designs, (a) design 1: MXene is used as an absorptive plasmonic layer sandwiched between the silica as a spacer layer and substrate with the Si nanodisk. The silicon nanoresonator has radius (r_{out}) of 268 nm and comprises a thorough air channel of radius (r_{in}) 80 nm. Other design parameters are the thickness, t_{Si} = 242 nm; the periodicity, Λ = 865 nm; the thickness of SiO_2 spacer layer (t_{SiO_2}), 200 nm; and the thickness of the MXene layer (t_{mx}), 90 nm. (b) Design 2: MXene is used as a nanoresonator. The design configuration consists of a composite nanodisk resonator, made from MXene, SiO_2, and Si, placed on a silica substrate. The composite nanodisk also has an air channel similar to design 1. The silica space layer thickness, t_{SiO_2} = 320 nm, while other parameters are similar to design 1. In both the design configurations, the air channel offset in the x direction is quantified by Δs.

and t_{SiO_2} = 320 nm in design 2. For designs 1 and 2, the amorphous Si is considered, with its refractive index taken from Pierce and Spicer.[69] The dielectric spacer and substrate have a constant refractive index of 1.44. Here, titanium carbide MXene is selected as the plasmonic film material. Ti_3C_2 is one of the most investigated MXenes since its discovery, owing to its high conductivity and stability. The spectral dependence of the real and imaginary parts of the dielectric permittivity of MXene is adopted from a paper by Hazan *et al.*[70] At the interface, MXene thin film can exhibit surface plasmon polaritons (SPPs). However, in a structured nanoresonator, localized surface plasmon resonance can be observed in the near-IR and mid-IR, as the real part of the permittivity is negative. It is found that the wavelength at which the negative permittivity originates decreases with the increase in the thickness of the MXene film. Therefore, thick MXene films exhibit significant metallic behavior.[71] The optical properties of MXene crucially depend on film thickness.

Figures 2(a)–2(f) illustrate various intermediate steps toward hybrid metasurface designs. For every intermediate design step, spectral responses are obtained and plotted in Fig. 2. In design 1, a highly reflective nanostructure is combined with a plasmonic film to achieve maximum absorption, as shown in Fig. 2(c). As illustrated in Figs. 2(b) and 2(e), when the metasurface without MXene is illuminated normally, it functions solely as a perfect reflector. While designing this metasurface, the concept of symmetry-protected quasi-BICs has been used. Since tuning the asymmetry parameter of quasi-SPBIC can achieve a high Q-factor, it can be used to create narrowband absorbers by controlling the radiative losses between the dielectric and MXene, thereby controlling their coupling. The MXene layer acts as a thin metallic film, and at normal incidence, it strongly reflects and weakly absorbs, with finite transmission. The MXene-dielectric metasurface separated by a spacer layer exhibits high absorbance when illuminated from the top upon (Si side), which is referred to as forward illumination. When the same system is illuminated from the substrate side (backward illumination), the absorbance is reduced, and transmittance remains the same; the reflectance is enhanced (see Fig. S9 in the supplementary material). The role of the spacer is to prevent the mode distortion.[44] In case of design 2, the MXene disk alone acts as a plasmonic resonator at normal incidence; it strongly absorbs ~50% and weakly reflects with finite transmission, as shown in Fig. 2(d). When the dielectric metasurface is combined with the MXene disk separated by a spacer disk, the resonant cavity exhibits high absorbance (forward illumination), achieved by tuning the air channel position as shown in Fig. 2(f). In case of backward illumination, absorption is reduced, while the reflection exhibits a peak with negligible transmittance at the resonant wavelength (see Fig. S9 in the supplementary material). In both designs, the transmittance is the same for both illuminations, indicating that the designs are reciprocal. However, their reflectance and absorbance differ under both forward and backward illumination because the material arrangement is different on the two sides of the metasurface, implying that both designs exhibit asymmetric responses. In addition, apart from the resonant wavelength, the transmittance is nonzero, indicating that both designs fall in the category of the two-port resonator system.

The proposed MXene-dielectric hybrid metasurface absorbers can be investigated using a generalized two-port temporal coupled-mode theory (TCMT) framework. Since both designs exhibit finite

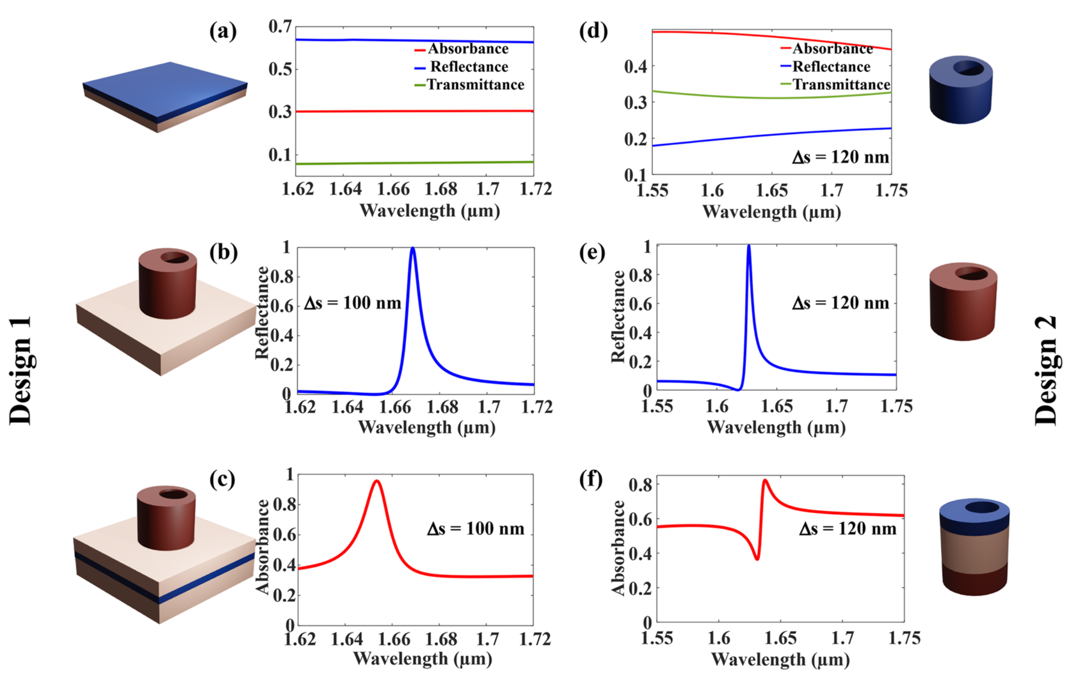

FIG. 2. Comparison between the optical responses of both designs. Design 1: Optical response of (a) a thin layer of MXene, (b) only a Si nanodisk, and (c) a hybrid nanostructure over the silica substrate. Design 2: Optical response of (d) MXene nanodisk, (e) Si nanodisk, and (f) hybrid composite nanodisk without substrate.

APL Eng. Phys. **1**, 036101 (2026); doi: 10.1063/5.0332754

transmission, they cannot be treated as ideal one-port absorbers. Instead, both designs are modeled as reciprocal but vertically asymmetric two-port resonant systems. In this notation, port 1 represents the top-side illumination port, while port 2 represents the substrate-side port.

For forward illumination, the reflection and transmission coefficients are S_{11} and S_{21}, respectively. Therefore, the forward absorbance is calculated as $A_{\mathrm{fwd}} = 1 - |S_{11}|^2 - |S_{21}|^2$. For backward illumination, the reflection and transmission coefficients are S_{22} and S_{12}, respectively. Therefore, the backward absorbance is $A_{\mathrm{bwd}} = 1 - |S_{22}|^2 - |S_{12}|^2$. Since the designs are reciprocal, $S_{21} = S_{12}$, the geometries are vertically asymmetric, $S_{11} \neq S_{22}$. Consequently, the forward and backward absorbance can be different $A_{\mathrm{fwd}} \neq A_{\mathrm{bwd}}$. This directional absorption asymmetry is an important signature of an asymmetric two-port resonant absorber. Using the two-port temporal-coupled mode theory (given in Sec. S8 of the supplementary material), the absorbance curve can be fitted to obtain the radiative and non-radiative quality factors for both designs. The fitted plot in Fig. S10 of the supplementary material shows that the fitted curve closely follows the simulated data. In both the designs, the following are the radiative and non-radiative decay rates: $\gamma_{r,design1} = 0.345$, $\gamma_{n,design1} = 0.329$, $\gamma_{r,design2} = 0.455$, and $\gamma_{n,design2} = 0.032$. In design 1, $\mathrm{RMSE}_{for,\,design1} = 9.519 \times 10^{-3}$ and $R^2_{for,design1} = 0.997$ and for design 2, $\mathrm{RMSE}_{for,\,design2} = 1.687 \times 10^{-3}$ and $R^2_{for,design2} = 0.999$.

The total quality factor (Q_{total}) of a particular mode can be calculated as[28]

$$\frac{1}{Q_{total}} = \frac{1}{Q_{rad}} + \frac{1}{Q_{non-rad}}, \tag{1}$$

where Q_{rad} is the radiative Q-factor in the absence of material and scattering losses, $Q_{rad} = \omega_0/2\gamma_r$, where γ_r is the radiative decay rate. Note that scattering losses may arise from the fabrication imperfections, finite array size, and surface roughness. In simulations, scattering loss is neglected, while the material loss contributes to the non-radiative Q-factor, $Q_{non-rad} = \omega_0/2\gamma_n$, where γ_n is the non-radiative decay rate. In simulations, periodic boundary conditions are used along the x and y axes. In contrast, perfectly matched layer boundary conditions are used along the z axis of the unit cell. It must be noted that the normal incident and the y-polarized light have been considered in both cases. In addition, eigenmode analysis is done to obtain the quality factor for both the radiative and non-radiative cases in both designs.

III. RESULTS AND DISCUSSION

A. Reflective metasurfaces without MXene

The proposed design of the nanoresonator (air hole in nanodisk) possesses C_{2v} symmetry in the xy plane when the air channel is not displaced from the center, and there is no substrate supporting an ideal SPBIC. The presence of substrate breaks the out-of-plane symmetry. Since the nanodisk is subwavelength and has zeroth-order diffraction, which is forbidden due to in-plane symmetry, the system will still exhibit ideal SPBIC.[72] Interestingly, the symmetry in the $x = 0$ plane is also broken when the air channel is displaced from the center by Δs such that the symmetry C_{2v} converts to C_s. Due to this symmetry breaking, the spectral resonance feature that was not observed in the spectral response becomes prominent as a Fano resonance. For the optimized parameters mentioned above, the structure exhibits only one mode, a symmetry-protected quasi-BIC named quasi-SPBIC. In case of zero offset of air-channel (i.e., $\Delta s = 0$) in the metasurface, no resonance occurs for y-polarized normal incidence, indicating complete decoupling of the mode with the incidence light [marked as the white circle in Fig. 3(a)]. As soon as the air-hole position in the nanoresonator is shifted, i.e., an increase in Δs, the in-plane symmetry is broken, and the resonance appears in the reflectance spectrum, as shown in Fig. 3(a), which is mainly due to enhanced coupling between the incidence light and the radiating mode. This also increases the resonance linewidth. Figure 3(b) shows the complete spectrum, i.e., reflectance, transmittance, and absorbance at $\Delta s = 100$ nm. We can observe how a lossless Si metasurface acts as a perfect reflector at $\lambda = 1.67$ μm with no absorption. The lossless Si contributes to the radiative Q-factor as there is no material loss in Si in the near-IR. Hence, the total Q-factor is driven by Q_{rad} such that with an increase in structural perturbation (Δs), the Q-factor decreases. When the $\Delta s = 100$ nm, the metasurface has a Q-factor of ≈261. The Q-factor exhibit the inverse quadratic relation with the asymmetry, Δs as $Q = k/\alpha^2$, where k is the proportionality constant dependent on metasurface design and α is asymmetry parameter given as $\alpha = \Delta s/r_{out}$ or $Q = kr_{out}^2/\Delta s^2$ as shown in Fig. 3(d).[73] The presence of substrate exhibits as a red shift in resonant wavelength, and the quality factor is less compared to the no substrate case when Δs is varied. The details are presented in Fig. S3 (Sec. S4) of the supplementary material.

Similarly, if the in-plane symmetry remains intact and the wavevector is varied along the x axis or the y axis, it is observed from the band diagram shown in the inset of Fig. 3(d) that SPBIC converts to quasi-SPBIC with a red shift in the wavelength since varying wavevector induces the asymmetry with respect to the incident light in momentum space. In addition, the Q-factor tends toward infinity at the Γ point, which means that the BIC is preserved for normal incidence on the symmetric structure. However, SPBIC converts to quasi-SPBIC as the angle of incidence changes and the symmetry is broken. The near-field distribution of electric and magnetic fields, as well as the Cartesian multipole decomposition, reveals the quasi-SPBIC resonance characteristics. The incident light-induced polarization has also been incorporated into the calculation of the scattered power for all multipole moments of a meta-atom (nanoresonator) unit cell. The scattered power of each multipole can be calculated from equations provided in the supplementary material (Sec. S1). Here, ED is an electric dipole, TED is a toroidal electric dipole, MD is a magnetic dipole, EQ is an electric quadrupole, TEQ is a toroidal electric quadrupole, MQ is a magnetic quadrupole, EO is an electric octupole, and MO is a magnetic octupole, respectively. Each mode of a nanoresonator is composed of several multipoles and contributes to far-field radiation. However, in the case of symmetry-protected BICs, the dominant component of the multipole moment is along the direction of incident light, preventing them from coupling with each other. In this particular study, the magnetic dipole moment of the mode aligns to the z axis ($\mathrm{MD_z}$) as its dominant component does not radiate in the far field. In contrast, the effect of other moments is minimal.[74] As a result, the nanoresonator forms an ideal BIC. When the symmetry is perturbed, for example, at $\Delta s = 100$ nm, other multipole moments also become strong, and the mode becomes leaky in the far field. It is observed from Fig. 3(c)

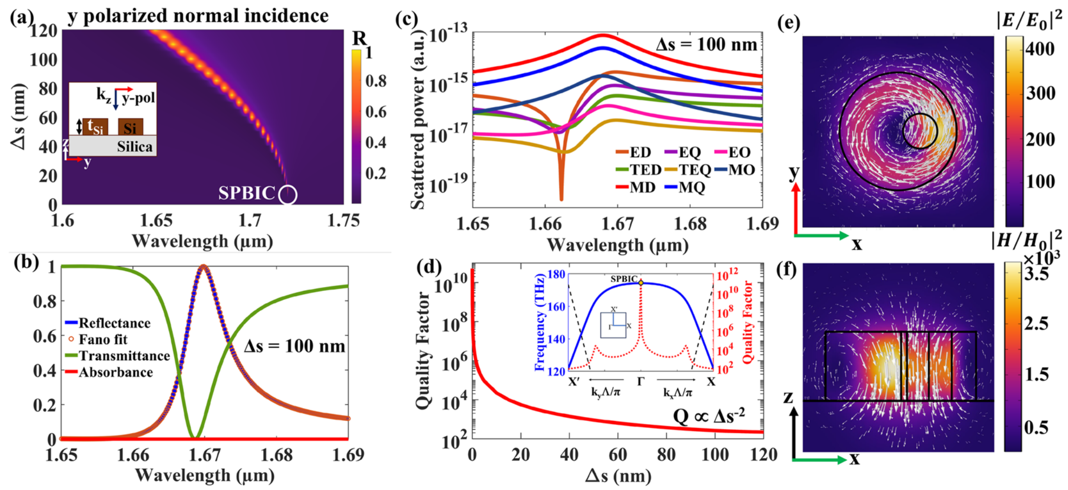

FIG. 3. Spectral characteristics of Si nanodisk resonator with an offset air-channel. (a) Reflectance plot for various offset (Δs) values of air-channel in the absence of MXene layer, constituting quasi-SPBIC for y polarized normal incident. The inset shows the cross section of the geometry in the yz plane without MXene. (b) Spectral response with the Fano fit. (c) Multipolar component of the quasi-BICs resonance. (d) Quality factor for various Δs. (e) Electric field intensity distribution and (f) magnetic field intensity distribution along with the field vector in the near-field. For (b)–(f), graphs are for Δs = 100 nm, except for (d).

that the MD and MQ are dominant, whereas other multipoles also exhibit peaks at the resonant wavelength. Thus, the SPBIC transforms into a radiating quasi-SPBIC with high reflectance. The near-field distributions of the electric and magnetic fields shown in Figs. 3(d) and 3(e) also confirm MD as a dominant mode, where the circulating electric field gives rise to the out-of-plane magnetic field in the xy plane.

B. Absorptive metasurface with MXene

The absorption in the Si nanodisk can be enhanced by combining it with the lossy material. To achieve this, we have examined two design aspects, as illustrated in Fig. 1.

1. Spectral absorption characteristics of design 1

The absorption in the reflective metasurface of design 1, as discussed earlier, can be enhanced by combining the dielectric metasurface with a plasmonic layer, which is 90 nm thick MXene layer and a spacer layer SiO_2 of thickness, t_{SiO_2} = 200 nm, as shown in the schematic cross section of the design in Fig. 4(a). The light absorption in the dielectric metasurface is mainly controlled by the three parameters (i) asymmetry parameter, Δs, (ii) thickness of spacer layer, t_{SiO_2}, and (iii) thickness of MXene layer, t_{mx}. Due to plasmonic behavior in the wavelength of interest, MXene introduces a necessary material loss for the metasurface to achieve absorption and prevent light transmission. For y-polarized normal incidence, the silicon nanoresonator (nanodisk with air channel) with in-plane symmetry, along with MXene, does not exhibit absorption [Fig. 4(b)] as the MD mode fails to couple with the incident light. In addition, the radiative Q-factor is significantly higher than the non-radiative Q-factor. As the value of Δs increases, the absorption increases, reaching maximum absorption around Δs = 100 nm. Subsequently, absorption decreases for a decreasing value of Δs as depicted in Fig. 4(b). It must be noted that the absorption remains ≈95% even if Δs changes by ±20% for fixed t_{SiO_2} and t_{mx}, suggesting a fabrication-tolerant design with respect to changes in air-hole dimensions.

We use eigenmode analysis to calculate the radiative Q-factor by assuming that the imaginary part of the refractive index of the MXene layer is zero for various values of Δs. Subsequently, the total Q-factor is calculated, accounting for the MXene layer's loss. The non-radiative Q-factor is derived using the relationship specified in Eq. (1). From Fig. 4(c), it is observed that Q_{rad} decreases as Δs increases nearly follows the inverse quadratic relation with respect to Δs with a slope estimate of −1.914 (see Fig. S4 in the supplementary material Sec. S5), whereas $Q_{non-rad}$ remains almost constant, as it mainly depends on the material loss and the thickness of the MXene layer. At Δs = 100 nm, both the $Q_{rad} \approx Q_{non-rad}$ indicate the critical coupling such that light does not scatter into the surrounding medium and almost perfect absorbance is achieved.

The hybrid metasurface (design 1) exhibits an absorbance peak of 95.6%, transmittance of 0.04%, and minimal reflectance when Δs = 100 nm, as shown clearly in Fig. 4(d). The metasurface yields a total Q-factor of 129. The MXene film not only behaves as a reflector but also absorbs and transmits a certain fraction of light, as depicted in Fig. 2(c). This characteristic persists during the interaction of light with the MXene film, the Si nanodisk, and the dielectric spacer.

The multipole decomposition technique facilitates the analysis and deeper understanding of the role of multipole moments in absorption. In the analysis, it was observed that magnetic multipoles (MD, MQ, and MO) exhibit a peak at a wavelength of 1653 nm [Fig. 4(e)], even in the absence of MXene. On the other hand, the electric multipole moments (ED, EQ, except EO) display a dip in the scattered power plot, indicating reflectance suppression. This observation becomes more evident when examining the phase spectrum of the multipole moment [Fig. 4(f)], where the magnetic and electric multipoles exhibit opposite slopes, suggesting the destructive interference that suppresses backward scattering (i.e., reflectance).

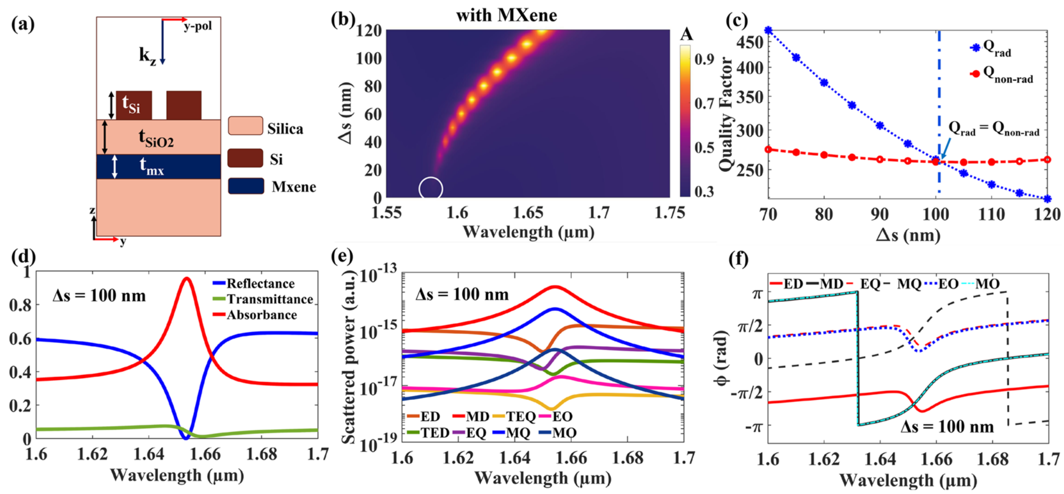

FIG. 4. (a) Cross section of the geometry in the yz plane with MXene layer as an absorptive thin film, (b) absorbance surface plot, (c) radiative and non-radiative quality factor for various Δs values. (d) Spectral (transmittance, reflectance, and absorbance) characteristics at Δs = 100 nm. (e) Multipole contributions when the metasurface is kept in the air for Δs = 100 nm. (f) Phase plots of various multipole (ED, MD, EQ, MQ, EO, and MO) moments.

The suppression of reflectance and blocking of transmission result in high absorbance at λ = 1653 nm.

The plasmonic behavior of MXene can be significantly improved by increasing the thickness of the MXene film. As deduced in Fig. 5(a), the resonant wavelength experiences blue shift when the MXene thickness increases from 50 to 90 nm, while SiO_2 thickness is fixed at 200 nm. In addition, the absorbance approaches unity, while the transmission approaches nearly zero. As the MXene film thickness increases, the transmission becomes minimal, potentially resulting in perfect absorbance in the metasurface. Since the interlayer coupling between the MXene layers is enhanced, the conductivity of the MXene film is also boosted, which, in turn, controls the non-radiative losses of the metasurface. The addition of a spacer layer significantly enhances absorption by forming a cavity between the dielectric metasurface and the MXene film, leading to destructive interference and suppression of backward scattering. By varying SiO_2 thickness, the optimum value corresponding to nearly perfect absorption is determined, as shown in Fig. 5(b).

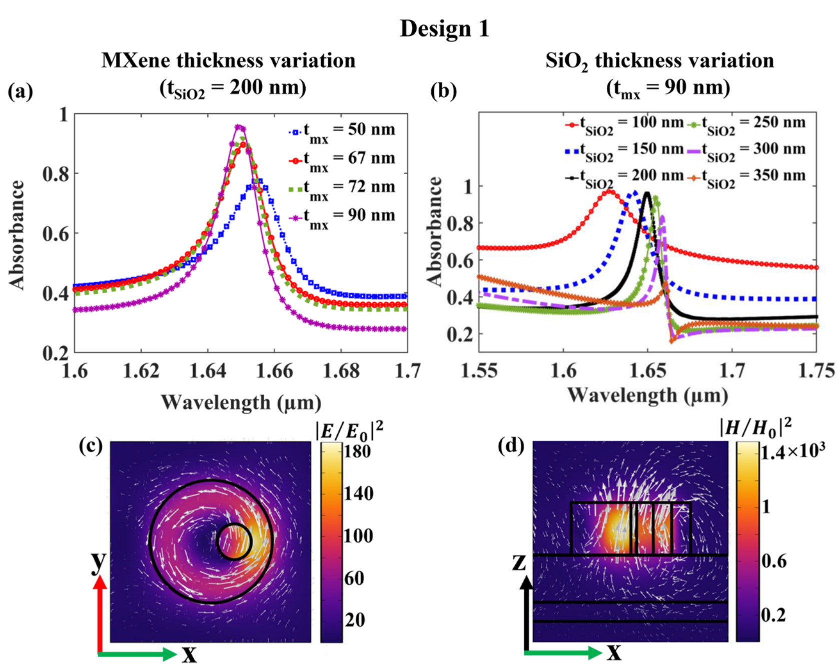

FIG. 5. (a) Effect of MXene layer thickness when spacer layer is fixed to t_{SiO_2} = 200 nm. (b) Impact of spacer layer thickness for a fixed MXene layer of t_{mx} = 90 nm. (c) Electric and (d) magnetic field distributions along with vector plot at λ = 1653 nm for t_{mx} = 90 nm and t_{SiO_2} = 200 nm.

At t_{SiO_2} = 200 nm, design 1 exhibits maximum absorbance with a total Q-factor of 129. Conversely, broadband behavior is observed at t_{SiO_2} = 100 nm. The absorption reduces when the thickness decreases from 200 nm. As previously noted, the absorption performance of design 1 demonstrates significant structural robustness. A ±20% variation in the thickness of the SiO_2 layer (t_{SiO_2}) has a negligible impact on performance, with absorption maintaining a high level of ≈95% when Δs and t_{mx} are held constant. Furthermore, even when both Δs and t_{SiO_2} are adjusted simultaneously within a ±20% range (with t_{mx} remaining fixed), the absorption remains remarkably stable and does not fall below ≈94%. These findings are further detailed in Fig. S7 of the supplementary material. The near-field distribution of electric and magnetic fields at the absorption wavelength is illustrated in Figs. 5(c) and 5(d), respectively. It is observed that near-field electric field lines maintain a configuration similar to that discussed earlier. However, the magnetic field lines in the xz plane are slightly tilted away from the z axis, indicating energy confinement in the spacer region.

2. Spectral absorption characteristics of design 2

So far, we have established that the absorption in the design 1 metasurface is mainly driven by the structural asymmetry that gives rise to a quasi-BIC, the losses associated with the MXene, and the spacer layer. In design 2, MXene nanodisk is combined with SiO_2 and Si nanodisk, resulting in high absorption. MXene, being a plasmonic material in near-infrared (NIR), may exhibit LSPR in NIR when nanostructuring is done.[68] On the contrary, in the studied design 2, the MXene is so thin (=90 nm) that it yields broadband absorption of ~50% in the wavelength range of interest.

As established earlier (see Fig. 3), Si nanodisk exhibits reflectance when there is no material loss involved under y-polarized normal incidence. When MXene is coated on silica-Silicon nanodisk with the presence of an air hole at the center [see Fig. 6(a)], the metasurface does not exhibit a narrow absorption resonance. However, as the air channel shifts by Δs in the x direction, the BIC mode converts to QBIC with a Fano lineshape, as observed from Fig. 6(b). The absorption increases with the increase in Δs and becomes maximum (≈85%) at Δs = 120 nm (λ = 1.66 μm). The spectral resonance at this wavelength shows a Q-factor of 184. Any further rise in Δs decreases the absorption, as observed from Fig. 6(b). It is also observed from Fig. 6(c) that the difference between the peak and the dip of the Fano resonances in absorption is ~40% at λ = 1.655 μm with negligible transmission and ~15% reflection, whereas in the vicinity of the resonance, the design 2 exhibits a constant absorption of nearly ~50%, which is in contrast with design 1. The absorption is mainly governed by the magnetic dipole moment as observed in Fig. 6(d). The dip and peak of the absorbance resonance in Fig. 6(c) originate due to the destructive and constructive interference between the multipoles of the Si and MXene nanodisk, which is discussed in detail in Sec. S2 of the supplementary material. Through eigenmode analysis and Fano fitting, the total Q-factor is calculated and shown in Fig. 6(e), along with the maximum absorbance with respect to the air-channel shift. It is observed that the maximum absorption occurs at a cost of a low Q-factor, when the shift is nearly Δs = 120 nm. For design 2, the system maintains relatively high efficiency despite geometric variations. When Δs varies within ±20% (while keeping t_{SiO_2} and t_{mx} constant), the peak absorption of ≈85% decreases to 80%. Furthermore, if the simultaneous fluctuations of ±20% in both t_{SiO_2} and Δs (at a fixed t_{mx}) occur, the absorption further drops to ≈75%. The effect of tolerance on performance is illustrated in Fig. S8 of the supplementary material. To attain the high-Q resonance, absorption should be compromised. The increase in absorption with an increase in the asymmetry parameter implies that the strong coupling occurs between the non-radiative losses of the MXene and the radiative losses of the quasi-BIC resonance. Since MXene has been used as a

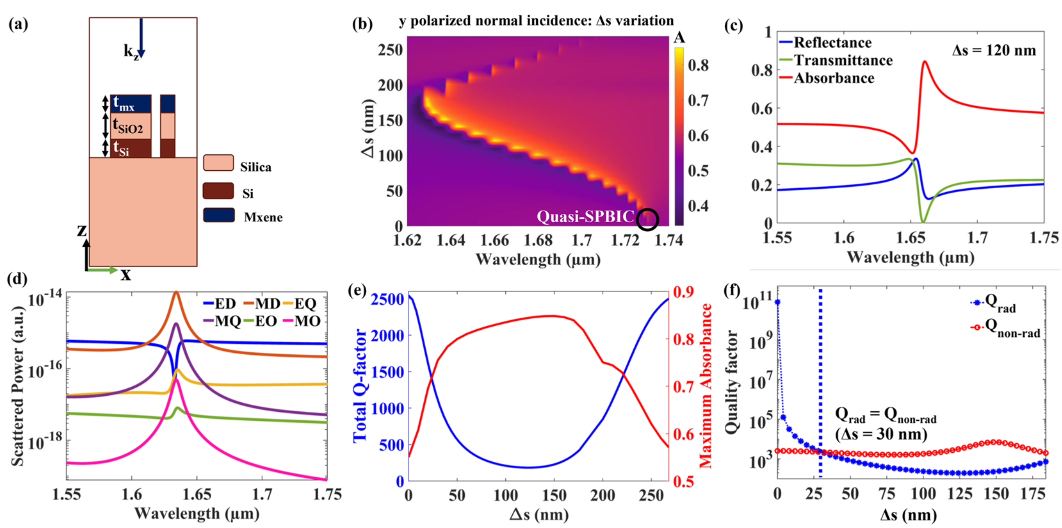

FIG. 6. (a) Cross section of the geometry in the xz plane with MXene on top of nanodisk (design 2), (b) absorbance plot for various values of air-channel shift, (c) spectral (transmittance, reflectance, and absorbance) characteristics at Δs = 120 nm, (d) multipole contributions in the absence of substrate at Δs = 120 nm. (e) Total quality factor and maximum absorbance, and (f) radiative and non-radiative quality factors for various Δs values.

nanodisk rather than a thin film (design 1), the entire configuration functions as a two-port system. From the radiative and non-radiative Q-factor plot [Fig. 6(f)], this design exhibits ≈50% absorption when $Q_{rad} = Q_{non-rad}$, which occurs at Δs = 30 nm, indicating a critically coupled state. It is to be noted that even if the air channel is not introduced and the MXene remains a complete nanodisk, design 2 still exhibits ≈70% absorption as shown in the supplementary material Sec. S9 (Fig. S11).

When the MXene thickness is changed from 50 to 72 nm, while other parameters are fixed, it is found that absorption increases for a fixed spacer thickness of t_{SiO_2} = 320 nm [Fig. 7(a)] but decreases after 72 nm without any shift in resonance wavelength. In addition, the absorption becomes ≈80% or larger for any MXene thickness as considered in the present case. The maximum absorption of ~90% occurs at t_{mx} = 72 nm. To further enhance the absorption in such a hybrid design, structural parameters can be fine-tuned or better optimized through an optimization algorithm. It is noteworthy to state that the spacer plays a very important role in achieving high absorption, more specifically for design 2 hybrid metasurface, as illustrated in Fig. 7(b), where the absorption is significantly enhanced due to the momentum matching between the plasmon of the MXene disk and the photonic modes in the Si disk. With the increase in the t_{SiO_2}, viz., from 150 to 350 nm, the resonant wavelength experiences a red shift, while the absorption first increases with an increase in thickness and attains a maximum of ≈87.6% at 250 nm and then starts decreasing. However, it is noteworthy that the absorption remains ≈80% or greater for a thickness range of 150–350 nm. This fact can further be validated by the electric field distribution [Fig. 7(c)], which mainly confines at the periphery of the Si nanodisk and circulates clockwise in the x–y plane. The circulating electric field produces an out-of-plane magnetic field, as shown in Fig. 7(d). Figure 7(e) confirms the presence of the electric field at the edges of the MXene disk and in the air channel, affirming the formation of LSPR. In addition, note that the electric field in the SiO_2 disk primarily concentrates the air channel, facilitating the coupling between the modes of MXene and the Si nanodisk.

When MXene is replaced with the gold in both the designs keeping all the geometrical parameters constant, it is observed that in the case of design 1, absorption reaches a maximum of 38% at a resonance wavelength of 1.688 μm, while in the case of design 2, there is negligible absorption at resonance wavelength of 1.728 μm (see supplementary material Fig. S2), which is less than that of MXene. Hence, this implies that, under the present scenario, MXene performs better than gold, as it has a high surface adsorption capacity at room temperature, which is helpful for sensor design. In addition, it is evident that loss-coupling engineering plays an important role when plasmonic materials are used to achieve near-unity absorption.

While the present work is a purely numerical study, the proposed designs have realistic dimensions and materials. An in-depth analysis of both designs reveals that they exhibit a tolerance of ±20% for the asymmetry parameter, MXene thickness, and spacer layer thickness, yielding an absorption of 80% or greater. Moreover, the designs can be easily fabricated, as silicon nanodisks with an off-center air hole can be patterned using electron-beam lithography or focused-ion-beam milling, techniques commonly employed for metasurface designs. Similar asymmetric dielectric nanostructures have been experimentally demonstrated in recent literature.[75] The integration of MXene layers is a new concept, but it is feasible: MXene (Ti_3C_2) can be deposited as a thin film or patterned at the nanoscale on dielectric substrates. In design 1, MXene is used as a continuous thin film coating between the SiO_2 substrate and the spacer layer. The proposed design can be fabricated using a combination of spray coating, low-temperature SiO_2 deposition, Si deposition, and electron beam lithography. A thin uniform layer of MXene (t_{mx} = 90 nm) can be deposited over a cleaned SiO_2 substrate through spin-coating or spray-coating techniques.[76] In these

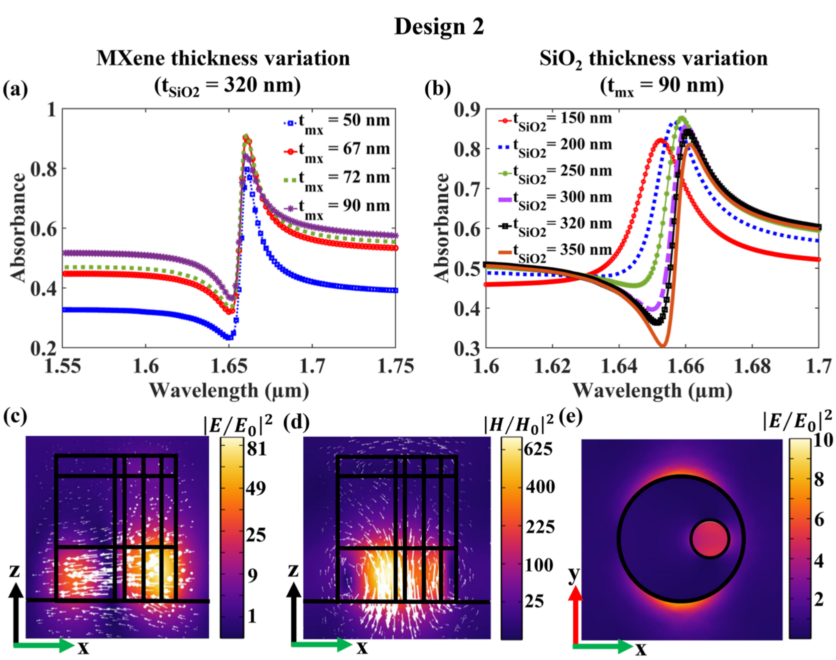

FIG. 7. Parametric study of design 2 hybrid metasurface, (a) effect of MXene layer thickness when the spacer layer thickness is fixed to 320 nm, (b) effect of spacer layer thickness for 90 nm thick MXene layer, (c) electric field, (d) magnetic field distributions and the vector plot in xz-plane, and (e) electric field distribution in MXene aided nanodisk in xy-plane at λ = 1653 nm when t_{mx} = 90 nm and t_{SiO_2} = 320 nm.

techniques, the thickness can be controlled by adjusting the solution concentration and the number of coating cycles. In addition, the substrate is mildly heated to promote rapid solvent evaporation and improve film uniformity and then dried either under vacuum or in an inert atmosphere to remove residual solvent and moisture. Since MXene is prone to oxidation and damage at high temperatures, the SiO_2 spacer is preferably deposited at low temperature, such as by thermal atomic layer deposition (ALD). Using ALD, a thin layer of 5–10 nm can be deposited first such that it can protect the MXene surface and enables uniform subsequent oxide growth. The remaining SiO_2 spacer thickness can then be obtained either by continuing ALD or by using low-temperature remote plasma-enhanced chemical vapor deposition (PECVD)/low-power PECVD, while avoiding direct oxygen plasma exposure to the MXene. After achieving the required SiO_2 spacer thickness, a silicon layer is deposited on top of the spacer using a low-temperature PECVD or sputtering process. The Si nanodisk array with air holes is then fabricated by electron-beam lithography (EBL). In design 2, the MXene is a nanodisk resonator on each Si/SiO_2 pillar. After depositing the Si and SiO_2 layers, the MXene layer is deposited through the above-mentioned technique. Then EBL is done, followed by etching (or lift-off), which defines the MXene nanodisk structure. This layered etching approach, though challenging, has been successfully implemented in other hybrid metasurface designs.[36] It is to be noted that for small variations in temperature, such as ±10 °C from the room temperature, the change in wavelength is negligible as shown in Sec. S6 of the supplementary material (Fig. S6).

C. Application of designed metasurface as methane gas sensor

Refractive index-based sensing has been widely used in various applications to detect precise changes in the refractive index of the surrounding medium. This method relies on the interaction between light and matter; specifically, the sensitivity of the evanescent waves around the metasurface induces changes in the refractive index of the surrounding media.[77] The primary challenge in designing a highly sensitive device is effectively responding to resonances influenced by near-field coupling effects. The sensors' performance is assessed using specific criteria, such as selectivity, sensitivity, and FOM. Both sensitivity and FOM are defined as follows:[77,78]

$$S = \Delta\lambda/\Delta n, \tag{2}$$

$$FOM = \frac{S}{FWHM}, \tag{3}$$

where $\Delta\lambda$ is the shift in wavelength, corresponding to a change in refractive index, Δn, and FWHM is the full-width half-maximum of the spectral resonance. The purpose of including the sensing analysis is to show that the MXene-based hybrid metasurface can also be employed for refractive-index detection through the spectral shift of its resonance. We investigate hybrid metasurface design 1, in which MXene behaves as a thin film and yields bulk refractive index sensing when the surrounding refractive index (n_{cy}) is varied from 1.4 to 1.45, as shown in Fig. 8(a). Here, design 1 was selected as a proof-of-concept structure to demonstrate the sensing ability of the hybrid metasurface, rather than as an exclusive or uniquely optimized sensing configuration. In this design, the MXene layer primarily introduces controlled optical loss, thereby enhancing the resonant absorptance peak and improving the visibility of the spectral feature. In numerical simulation or experiments, absorbance cannot be obtained directly; instead, it is calculated from the reflectance and transmittance spectra using $A = 1 - R - T$. Since design 1 tends toward a near one-port absorptive configuration, the transmittance is very small over the resonance region, and the absorptance can be approximately inferred from the reflectance response as $A \approx 1 - R$, after verifying that T remains negligible. Both reflectance and absorbance can be used to monitor the resonance shift due to varying refractive index, since they are for the

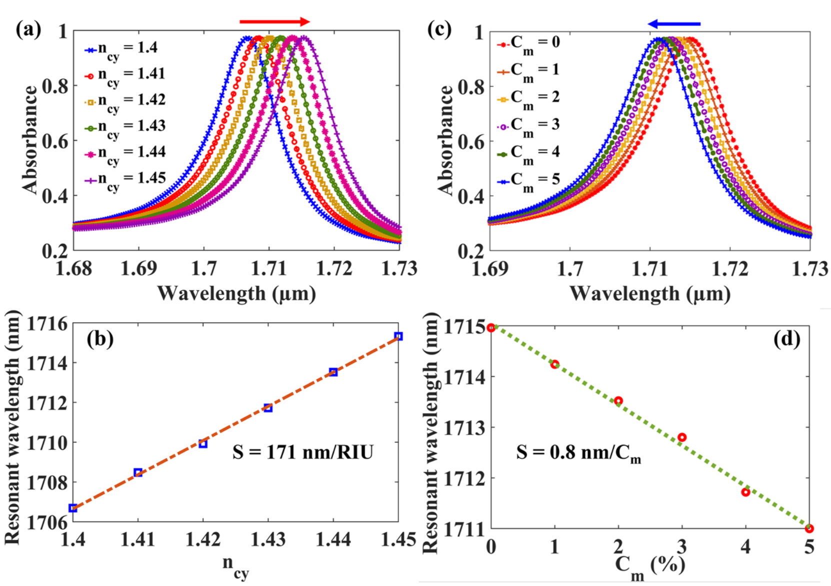

FIG. 8. (a) Absorbance plot dictating the refractive index sensing for a 400 nm thick analyte layer, (b) sensitivity plot for bulk refractive index sensing, (c) absorbance plot when a 400 nm thick Cryptophane-E doped polymer layer is exposed to different concentrations of methane gas. The blue arrow represents the blue shift in the spectral response. (d) Methane gas sensitivity plot for various gas concentrations.

TABLE II. Comparison of various methane gas sensors.

Reference	Structures	Type	Materials	S (nm/%)
85	Gold nanorings	LSPR	Au	1.02 nm/%
86	Si square rings	BIC	Si/SiO_2	1.03 nm/%
87	Si nanobar with air channel	Fano resonance	Si/SiO_2	0.608 nm/%
88	VO_2 square ring with slits	Fano resonance	VO_2/SiO_2	7.13 GHz/%
89	Nanodisk	Mie resonance	$Au/dielectric/Au/SiO_2$	
This work	Si hollow nanodisk	BIC	$Si/MXene/SiO_2$	0.8 nm/% or 81.5 GHz/%

same mode. However, the absorbance spectrum shows a positive, high-contrast peak that is easier to visualize and directly reflects the MXene-assisted resonant dissipation, whereas the corresponding reflectance spectrum shows a shallow peak. Thus, absorbance is used here primarily to clearly visualize the resonance shift and enhanced light–matter interaction. Numerical simulations indicate near-unity absorption of the incident electromagnetic field. To observe refractive index variation, a polymeric film is used as the analyte layer with a thickness of 400 nm. Figure 8(a) shows a clear redshift in the spectral response. The metasurface design 1 demonstrates a sensitivity of $S = 179$ nm/RIU and FOM = 17.56 RIU^{-1} for $\Delta n = 0.01$. In Fig. 8(b), it is evident that the average sensitivity is 171 nm/RIU. The sensitivity enhancement is attributed to the asymmetric excitation of both electric and magnetic resonances.

In the near-infrared region, methane gas exhibits two near-infrared vibrational absorption bands, $\nu_2 + 2\nu_3$ and $2\nu_3$, with corresponding absorption peaks in the wavelength range of 1330–1335 and 1650–1670 nm.[79] The methane gas absorption band at 1653 nm ($2\nu_3$) is significantly stronger by an order of magnitude and experiences minimal interference from other gases compared to the weaker ($\nu_2 + 2\nu_3$) band. This makes it highly suitable for direct spectroscopic sensing applications.[80] By designing the resonant absorption to coincide with the methane absorption band, selectivity can be further maximized while minimizing cross-sensitivity.

An effective method to enhance the selectivity and sensitivity of gas detection from mixtures is to use a gas-sensitive material on top of the metasurface. In the case of methane gas sensing, a gas-permeable polymer, such as polysiloxane doped with the Cryptophane-E, is one of the primary molecules that facilitates the interaction with methane gas.[81] Notably, Cryptophanes are the sole functional materials that exhibit a photosensitive response to methane.[82] In the presence of methane gas, the Cryptophane-doped polymer layer adsorbs the gas molecules, altering their dipole moments and, in turn, the polymer's refractive index. The metasurface's resonance peak is thereby shifted in proportion to the methane concentration, enabling us to quantify methane in the environment. However, crytophane, when it comes into contact with other gases, does not produce a similar effect. In practice, this means the proposed sensor is "tuned" to methane through both its material choice and its spectral response. Methane sensing is limited to the low-concentration regime relevant for early warning, below or around the lower explosive limit. Methane has a lower explosive limit of ~5% by volume in air, and the flammable range is commonly reported as ~5%–15% by volume;[83] therefore, practical methane detection should ideally occur before the concentration reaches 5%.

The refractive index n of Cryptophane-E doped polymer thin film variation with methane concentration C_m, which is the fractional methane concentration, is given as[84]

$$n = 1.448 - 0.46C_m. \tag{4}$$

The linear refractive-index relation used here was adopted from reported Cryptophane-E-based methane-sensing studies[84] and is not extrapolated beyond the concentration range considered in this work. Figure 8(c) illustrates the absorbance spectra of the hybrid metasurface design 1 for various concentration values of methane gas. As the methane gas concentration C_m increases, the resonance characteristics remain consistent, but the resonant wavelength shifts to shorter wavelengths. At very low methane concentration ($C_m = 0$), the Cryptophane-doped polymeric film behaves similarly to an analyte with a refractive index of 1.45. As the methane concentration increases by 1%, the resonance shifts to a shorter wavelength due to the reduced refractive index of the Cryptophane-E doped polymer layer. In this case, the expression for the sensitivity is modified to

$$S = \frac{\Delta\lambda}{\Delta C_m} = \frac{\Delta\lambda}{\Delta n}\frac{\Delta n}{\Delta C_m}, \tag{5}$$

where ΔC_m denotes the change in the methane concentration. When the methane gas concentration changes by 1%, the resonant wavelength is blue-shifted by 0.72 nm. The average sensitivity is 0.8 nm per 1% change in methane gas concentration with FOM = 0.07 per 1% change in methane concentration, as depicted in Fig. 8(d). Simulation results indicate enhanced methane sensitivity when Cryptophane E is incorporated into the hybrid metasurface. It can be observed from Table II that the methane sensitivity of the proposed work is comparable to, and in some cases even better than, that of the existing work.

IV. CONCLUSIONS

In this work, we demonstrated two novel MXene–dielectric hybrid metasurface absorbers that exploit symmetry-protected BIC physics to achieve narrowband, high-Q resonances suitable for methane detection in the near-infrared region. By carefully engineering the structural asymmetry and integrating MXene either as a thin plasmonic layer (design 1) or as a nanodisk resonator (design 2), we achieved strong light–matter interaction with near-unity absorption, viz., an absorbance of >90% with a Q-factor of 129 (design 1) and >80% absorbance with a Q-factor of 184 (design 2), confirming the controlled interplay between radiative and non-radiative loss channels for optimal performance. During the feasibility test, both designs exhibit a tolerance of ±20% for the asymmetry parameter, MXene thickness, and spacer layer thickness, achieving absorption of ≈80% or greater. A detailed TCMT mathematical framework facilitates the calculation of radiative and non-radiative decay rates for both the designs ($\gamma_{r,design1}$ = 0.345, $\gamma_{n,design1}$ = 0.329, $\gamma_{r,design2}$ = 0.455, $\gamma_{n,design2}$ = 0.032).

The gas-sensing capabilities of the designed metasurfaces have also been investigated for methane detection. The sensing functionality was further enhanced by incorporating a Cryptophane-E layer, whose high affinity for methane enables selective adsorption and modulation of the index. Numerical simulations revealed a bulk refractive index sensitivity of ~171 nm/RIU, a FOM of 17.56 RIU^{-1}, and a methane-specific sensitivity of 0.8 nm per unit concentration percentage, establishing the hybrid metasurface as a competitive platform for trace-level gas monitoring. The device operates around 1653 nm, precisely overlapping with the strong overtone absorption band of Methane, thereby maximizing selectivity and minimizing cross-sensitivity to other gases. The ultracompact hybrid metasurface design concepts can also be extended to other greenhouse gases for environmental monitoring, molecular spectroscopy, and photonic on-chip integration.

SUPPLEMENTARY MATERIAL

See the supplementary material for additional information about the Cartesian multipole decomposition method; detailed multipolar decomposition of design 2; comparison of MXene-Si hybrid metasurfaces with gold–Si hybrid metasurfaces; details on the substrate effects, radiative-Q scaling, temperature dependence, and fabrication-tolerance behavior through variations in MXene thickness, SiO_2 spacer thickness, and air-channel offset; development of the two-port TCMT model; and the graphs of the simulated forward/backward absorbance spectra.

ACKNOWLEDGMENTS

This research was supported by the Ministry of Science and Technology, Israel-India Grant No. 0006276 and DST Government of India, Vide No. DST/INT/ISR/P-34/2023.

AUTHOR DECLARATIONS

Conflict of Interest

The authors have no conflicts to disclose.

Author Contributions

Shubhanshi Sharma: Conceptualization (equal); Data curation (lead); Formal analysis (lead); Investigation (lead); Methodology (lead); Validation (equal); Visualization (equal); Writing – original draft (lead). **Monica Pradhan**: Conceptualization (equal); Formal analysis (supporting); Validation (supporting); Visualization (equal); Writing – review & editing (equal). **Aviad Katiyi**: Formal analysis (supporting); Visualization (supporting); Writing – review & editing (supporting). **Alina Karabchevsky**: Conceptualization (equal); Funding acquisition (equal); Project administration (supporting); Supervision (supporting); Writing – review & editing (equal). **Shailendra Kumar Varshney**: Conceptualization (equal); Funding acquisition (equal); Project administration (lead); Resources (lead); Software (lead); Supervision (lead); Writing – review & editing (lead).

DATA AVAILABILITY

The data that support the findings of this study are available from the corresponding author upon reasonable request.

REFERENCES

[1] A. Karabchevsky, A. Katiyi, A. S. Ang, and A. Hazan, "On-chip nanophotonics and future challenges," Nanophotonics **9**, 3733–3753 (2020).

[2] H.-H. Hsiao, C. H. Chu, and D. P. Tsai, "Fundamentals and applications of metasurfaces," Small Methods **1**, 1600064 (2017).

[3] M. Khorasaninejad and F. Capasso, "Metalenses: Versatile multifunctional photonic components," Science **358**, eaam8100 (2017).

[4] P.-Y. Chen, J. Soric, and A. Alù, "Invisibility and cloaking based on scattering cancellation," Adv. Mater. **24**, OP281–OP304 (2012).

[5] Q. Jiang, G. Jin, and L. Cao, "When metasurface meets hologram: Principle and advances," Adv. Opt. Photonics **11**, 518–576 (2019).

[6] J. Qin, S. Jiang, Z. Wang, X. Cheng, B. Li, Y. Shi, D. P. Tsai, A. Q. Liu, W. Huang, and W. Zhu, "Metasurface micro/nano-optical sensors: Principles and applications," ACS Nano **16**, 11598–11618 (2022).

[7] S. Lin, Y. Chen, and Z. J. Wong, "High-performance optical beam steering with nanophotonics," Nanophotonics **11**, 2617–2638 (2022).

[8] B. Sain, C. Meier, and T. Zentgraf, "Nonlinear optics in all-dielectric nanoantennas and metasurfaces: A review," Adv. Photonics **1**, 024002 (2019).

[9] T. Badloe, J. Mun, and J. Rho, "Metasurfaces-based absorption and reflection control: Perfect absorbers and reflectors," J. Nanomater. **2017**, 2361042.

[10] H. Wang, V. Prasad Sivan, A. Mitchell, G. Rosengarten, P. Phelan, and L. Wang, "Highly efficient selective metamaterial absorber for high-temperature solar thermal energy harvesting," Sol. Energy Mater. Sol. Cells **137**, 235–242 (2015).

[11] H.-Y. Cheng, M.-J. Ye, W.-R. Chen, C.-Y. Yang, S.-W. Chu, K.-P. Chen, and K.-H. Lin, "Large optical modulation of dielectric Huygens' metasurface absorber," Adv. Opt. Mater. **11**, 2300102 (2023).

[12] N. Liu, M. Mesch, T. Weiss, M. Hentschel, and H. Giessen, "Infrared perfect absorber and its application as plasmonic sensor," Nano Lett. **10**, 2342–2348 (2010).

[13] C. M. Watts, X. Liu, and W. J. Padilla, "Metamaterial electromagnetic wave absorbers," Adv. Mater. **24**, OP98–OP120 (2012).

[14] W. Li, U. Guler, N. Kinsey, G. V. Naik, A. Boltasseva, J. Guan, V. M. Shalaev, and A. V. Kildishev, "Refractory plasmonics with titanium nitride: Broadband metamaterial absorber," Adv. Mater. **26**, 7959–7965 (2014).

[15] J. Tian, Q. Li, P. A. Belov, R. K. Sinha, W. Qian, and M. Qiu, "High-Q all-dielectric metasurface: Super and suppressed optical absorption," ACS Photonics **7**, 1436–1443 (2020).

[16] H. Tao, N. I. Landy, C. M. Bingham, X. Zhang, R. D. Averitt, and W. J. Padilla, "A metamaterial absorber for the terahertz regime: Design, fabrication and characterization," Opt. Express **16**, 7181–7188 (2008).

[17] M. Pradhan, S. Sharma, S. Bhaktha BN, and S. K. Varshney, "Engineered pseudo and hybrid anapole states in a silicon nanoresonator metasurface," J. Opt. Soc. Am. B **40**, 986–993 (2023).

[18] S. Sharma, M. Pradhan, A. Yadav, and S. K. Varshney, "Visible to infrared dielectric metasurfaces and their applications," Indian J. Pure Appl. Phys. **61**, 568–588 (2023).

[19] C. W. Hsu, B. Zhen, A. D. Stone, J. D. Joannopoulos, and M. Soljačić, "Bound states in the continuum," Nat. Rev. Mater. **1**, 16048 (2016).

[20] E. N. Bulgakov and A. F. Sadreev, "Bound states in the continuum in photonic waveguides inspired by defects," Phys. Rev. B **78**, 075105 (2008).

[21] A. Pavlov, I. Zabkov, and V. Klimov, "Lasing threshold of the bound states in the continuum in the plasmonic lattices," Opt. Express **26**, 28948–28962 (2018).

[22] Y. Liang, K. Koshelev, F. Zhang, H. Lin, S. Lin, J. Wu, B. Jia, and Y. Kivshar, "Bound states in the continuum in anisotropic plasmonic metasurfaces," Nano Lett. **20**, 6351–6356 (2020).
[23] S. Han, L. Cong, Y. K. Srivastava, B. Qiang, M. V. Rybin, A. Kumar, R. Jain, W. X. Lim, V. G. Achanta, S. S. Prabhu, Q. J. Wang, Y. S. Kivshar, and R. Singh, "All-dielectric active terahertz photonics driven by bound states in the continuum," Adv. Mater. **31**, 1901921 (2019).
[24] A. Kodigala, T. Lepetit, Q. Gu, B. Bahari, Y. Fainman, and B. Kanté, "Lasing action from photonic bound states in continuum," Nature **541**, 196–199 (2017).
[25] Y. Plotnik, O. Peleg, F. Dreisow, M. Heinrich, S. Nolte, A. Szameit, and M. Segev, "Experimental observation of optical bound states in the continuum," Phys. Rev. Lett. **107**, 183901 (2011).
[26] D. C. Marinica, A. G. Borisov, and S. V. Shabanov, "Bound states in the continuum in photonics," Phys. Rev. Lett. **100**, 183902 (2008).
[27] Y. Yang, C. Peng, Y. Liang, Z. Li, and S. Noda, "Analytical perspective for bound states in the continuum in photonic crystal slabs," Phys. Rev. Lett. **113**, 037401 (2014).
[28] L. Cong and R. Singh, "Symmetry-protected dual bound states in the continuum in metamaterials," Adv. Opt. Mater. **7**, 1900383 (2019).
[29] S. Sharma, B. Lahiri, and S. Varshney, "Multispectral tunable symmetry-protected bound states in the continuum in all-dielectric split-ring resonator metasurfaces," J. Phys. D: Appl. Phys. **56**, 055104 (2023).
[30] C. Zhou, R. Jin, H. He, J. Huang, G. Li, and L. Huang, "Robust ultrahigh-Q resonances in tetramer metasurfaces through centroid symmetry protection and area conservation," Light: Sci. Appl. **15**, 84 (2026).
[31] K. Watanabe, T. Nagao, and M. Iwanaga, "Low-contrast BIC metasurfaces with quality factors exceeding 100,000," Nano Lett. **25**, 2777–2784 (2025).
[32] C. Zhou, M. Zhou, Z. Fu, H. He, Z.-L. Deng, H. Xiang, X. Chen, W. Lu, G. Li, and D. Han, "Ultrahigh-Q quasi-BICs via precision-controlled asymmetry in dielectric metasurfaces," Nano Lett. **25**, 5916–5924 (2025).
[33] K. Moriasa, H. Hasebe, H. Sugimoto, and M. Fujii, "Bound states in the continuum (BIC) in silicon nanodisk array on mirror structure: Perfect absorption associated with quasi-BIC below the bandgap," J. Appl. Phys. **133**, 173102 (2023).
[34] S. Wan, C. Qin, K. Wang, Y. Li, C. Guan, B. Lv, W. Li, and J. Shi, "Ultra-high quality perfect absorber based on quasi bound states in the continuum," J. Appl. Phys. **131**, 213104 (2022).
[35] Z. Li, L. Fan, H. Zhao, Y. Yan, and J. Gao, "Optical properties and application potential of a hybrid cavity compound grating structure," Opt. Express **30**, 7737–7749 (2022).
[36] D. Ray, T. V. Raziman, C. Santschi, D. Etezadi, H. Altug, and O. J. F. Martin, "Hybrid metal-dielectric metasurfaces for refractive index sensing," Nano Lett. **20**, 8752–8759 (2020).
[37] M. Luo, Y. Zhou, X. Zhao, Z. Guo, Y. Li, Q. Wang, J. Liu, W. Luo, Y. Shi, A. Q. Liu, and X. Wu, "High-sensitivity optical sensors empowered by quasi-bound states in the continuum in a hybrid metal–dielectric metasurface," ACS Nano **18**, 6477–6486 (2024).
[38] S. Lingala and S. Singarapu, "Switchable MXene–graphene metamaterial absorber for wideband shielding and dual-band biosensing in the THz regime," Opt. Eng. **64**, 117107 (2025).
[39] M. Saqlain, M. A. Baqir, and P. K. Choudhury, "MXene- and graphene-assisted THz metamaterial for cancer cells detection based on refractive index sensing," IEEE Trans. Nanotechnol. **23**, 652–657 (2024).
[40] H. Sun, L. Yang, X. Cao, B. Cai, Y. Cheng, H. Luo, and X. Li, "Terahertz perfect metasurface absorber based on groove-ring-shaped $Ti_3C_2T_x$ MXene for refractive index sensing application," IEEE Sens. J. **25**, 30845–30853 (2025).
[41] J. Wekalao and O. Elamri, "Dual-resonator MXene metasurface-based gas sensor with machine learning-enhanced surface plasmon resonance detection," Plasmonics **21**, 421 (2026).
[42] U. Arun Kumar, L. Jubair Ahmed, H. Kraiem, and T. Sheheryar, "MXene-BP-graphene metasurface terahertz biosensor for high-sensitivity detection of carcinoembryonic antigen and malaria histidine-rich protein II," Microsyst. Technol. **31**, 4037 (2025).
[43] A. A. Rifat, M. Rahmani, L. Xu, and A. E. Miroshnichenko, "Hybrid metasurface based tunable near-perfect absorber and plasmonic sensor," Materials **11**, 1091 (2018).
[44] J. Yu, B. Ma, R. Qin, P. Ghosh, M. Qiu, and Q. Li, "High-Q absorption in all-dielectric photonics assisted by metamirrors," ACS Photonics **9**, 3391–3397 (2022).
[45] J. Zhao, Y. Wang, Y. Zhu, W. Zhang, and Y. Yu, "Lithography-free flexible perfect broadband absorber in visible light based on an all-dielectric multilayer structure," Opt. Lett. **45**, 5464–5467 (2020).
[46] P. Yu, L. V. Besteiro, Y. Huang, J. Wu, L. Fu, H. H. Tan, C. Jagadish, G. P. Wiederrecht, A. O. Govorov, and Z. Wang, "Broadband metamaterial absorbers," Adv. Opt. Mater. **7**, 1800995 (2019).
[47] Y. Guo, X. Lv, C. Li, X. Wu, X. Wang, J. Wang, and K. Bi, "Double-layered ceramic disk-constructed all-dielectric Huygens metasurface perfect absorber," IEEE Trans. Antennas Propag. **72**, 6801 (2024).
[48] J. Liu, Y. Tan, D. Zhang, Q. Wen, Y. Liao, Z. Zhong, and T. Wen, "Plasmonic nanocomposite for active dielectric metasurface terahertz absorbers," IEEE Trans. Terahertz Sci. Technol. **13**, 381–388 (2023).
[49] M. A. Houran, M. Saqlain, and M. A. Baqir, "ITO-based UV dielectric metasurface absorber: Achieving polarization-insensitive operation," Europhys. Lett. **144**, 16001 (2023).
[50] J.-Y. Zong and M.-S. Cao, "Graphene-like MXene-based microwave absorbers and shields: Latest progress and perspectives," Mater. Today Phys. **43**, 101400 (2024).
[51] Y. Gogotsi, *MXenes: From Discovery to Applications of Two-Dimensional Metal Carbides and Nitrides* (CRC Press, 2023).
[52] F. M. Oliveira, J. Azadmanjiri, X. Wang, M. Yu, and Z. Sofer, "Structure design and processing strategies of MXene-based materials for electromagnetic interference shielding," Small Methods **7**, 2300112 (2023).
[53] Y. Zhang, J. Wu, L. Jia, D. Jin, B. Jia, X. Hu, D. Moss, and Q. Gong, "Advanced optical polarizers based on 2D materials," npj Nanophotonics **1**, 28 (2024).
[54] H. Saini, N. Srinivasan, V. Šedajová, M. Majumder, D. P. Dubal, M. Otyepka, R. Zbořil, N. Kurra, R. A. Fischer, and K. Jayaramulu, "Emerging MXene@metal–organic framework hybrids: Design strategies toward versatile applications," ACS Nano **15**, 18742–18776 (2021).
[55] Z. Ullah, M. Junaid, and I. Nawi, "Near-field and polarization control at terahertz with a 2D MXene/VO_2 phase change metasurface," Opt. Continuum **4**, 198–209 (2025).
[56] D. B. Lioi, P. R. Stevenson, B. T. Seymour, G. Neher, R. D. Schaller, D. J. Gosztola, R. A. Vaia, J. P. Vernon, and W. J. Kennedy, "Simultaneous ultrafast transmission and reflection of nanometer-thick $Ti_3C_2T_x$ MXene films in the visible and near-infrared: Implications for energy storage, electromagnetic shielding, and laser systems," ACS Appl. Nano Mater. **3**, 9604–9609 (2020).
[57] C. Hu, Z. Wei, L. Li, and G. Shen, "Strategy toward semiconducting $Ti_3C_2T_x$-MXene: Phenylsulfonic acid groups modified $Ti_3C_2T_x$ as photosensitive material for flexible visual sensory-neuromorphic system," Adv. Funct. Mater. **33**, 2302188 (2023).
[58] M. Khazaei, M. Arai, T. Sasaki, C.-Y. Chung, N. S. Venkataramanan, M. Estili, Y. Sakka, and Y. Kawazoe, "Novel electronic and magnetic properties of two-dimensional transition metal carbides and nitrides," Adv. Funct. Mater. **23**, 2185–2192 (2013).
[59] N. T. T. Phuong, L. H. Tho T. T. Nguyen, N. N. Nam, and K. T. L. Trinh, "Application of MXenes and their composites in plasmon-enhanced optical sensors," Sens. Actuators, A **363**, 114714 (2023).
[60] G. Zhu and Y. Zhang, "Properties of MXenes," in *Fundamental Aspects and Perspectives of MXenes* (Springer, 2022), pp. 37–52.
[61] Z. Cai and H. Kim, "Recent advances in MXene gas sensors: Synthesis, composites, and mechanisms," npj 2D Mater. Appl. **9**, 66 (2025).
[62] Y. Chen, Y. Ge, W. Huang, Z. Li, L. Wu, H. Zhang, and X. Li, "Refractive index sensors based on $Ti_3C_2T_x$ MXene fibers," ACS Appl. Nano Mater. **3**, 303–311 (2020).
[63] R. Singh, W. Zhang, X. Liu, B. Zhang, and S. Kumar, "WaveFlex biosensor: MXene-immobilized W-shaped fiber-based LSPR sensor for highly selective tyramine detection," Opt Laser. Technol. **171**, 110357 (2024).
[64] H. Li, K. Yang, H. Hu, C. Qin, B. Yu, S. Zhou, T. Jiang, and D. Ho, "MXene supported surface plasmon polaritons for optical microfiber ammonia sensing," Anal. Chem. **96**, 11823–11831 (2024).
[65] V. Pacheco-Peña, T. Hallam, and N. Healy, "MXene supported surface plasmons on telecommunications optical fibers," Light: Sci. Appl. **11**, 22 (2022).

[66]Y. Jia, T. Wu, G. Wang, J. Jiang, F. Miao, and Y. Gao, "Visible and near-infrared broadband absorber based on $Ti_3C_2T_x$ MXene-Wu," Nanomaterials **12**, 2753 (2022).
[67]W. Huang, X. Liu, Y. Zhou, S. Yang, W. Huang, Z. Chen, J. Feng, Z. Chen, X. Li, and X. Gui, "Inkjet-printing $Ti_3C_2T_x$ MXene nanosheet-based metamaterials for terahertz absorption," ACS Appl. Nano Mater. **7**, 15308–15316 (2024).
[68]K. Chaudhuri, M. Alhabeb, Z. Wang, V. M. Shalaev, Y. Gogotsi, and A. Boltasseva, "Highly broadband absorber using plasmonic titanium carbide (MXene)," ACS Photonics **5**, 1115–1122 (2018).
[69]D. T. Pierce and W. E. Spicer, "Electronic structure of amorphous Si from photoemission and optical studies," Phys. Rev. B **5**, 3017–3029 (1972).
[70]A. Hazan, B. Ratzker, D. Zhang, A. Katiyi, M. Sokol, Y. Gogotsi, and A. Karabchevsky, "MXene-nanoflakes-enabled all-optical nonlinear activation function for on-chip photonic deep neural networks," Adv. Mater. **35**, 2210216 (2023).
[71] C. K. Panda, S. M. Naqvi, H. G. Lee, T. Hassan, A. Iqbal, Y. S. Choi, K-Y. Choi, C. M. Koo, and J. Hwang, "Quantitative broadband optical spectroscopy of free-standing $Ti_3C_2T_x$ MXene films: Unveiling intrinsic bulk charge carrier dynamics," ACS Appl. Mater. Interfaces **17**, 69590–69599 (2025).
[72]Z. F. Sadrieva, I. S. Sinev, K. L. Koshelev, A. Samusev, I. V. Iorsh, O. Takayama, R. Malureanu, A. A. Bogdanov, and A. V. Lavrinenko, "Transition from optical bound states in the continuum to leaky resonances: Role of substrate and roughness," ACS Photonics **4**, 723–727 (2017).
[73]K. Koshelev, S. Lepeshov, M. Liu, A. Bogdanov, and Y. Kivshar, "Asymmetric metasurfaces with high-*Q* resonances governed by bound states in the continuum," Phys. Rev. Lett. **121**, 193903 (2018).
[74]Z. Sadrieva, K. Frizyuk, M. Petrov, Y. Kivshar, and A. Bogdanov, "Multipolar origin of bound states in the continuum," Phys. Rev. B **100**, 115303 (2019).
[75]C. Zhou, L. Huang, R. Jin, L. Xu, G. Li, M. Rahmani, X. Chen, W. Lu, and A. E. Miroshnichenko, "Bound states in the continuum in asymmetric dielectric metasurfaces," Laser Photonics Rev. **17**, 2200564 (2023).
[76]Y.-Z. Zhang, Y. Wang, Q. Jiang, J. K. El-Demellawi, H. Kim, and H. N. Alshareef, "MXene printing and patterned coating for device applications," Adv. Mater. **32**, 1908486 (2020).
[77]S. Sharma, R. Kumari, S. K. Varshney, and B. Lahiri, "Optical biosensing with electromagnetic nanostructures," Rev. Phys. **5**, 100044 (2020).
[78]Y. Ben-Ali, I. El Kadmiri, Y. Errouas, Z. Rahou, and D. Bria, "High sensibility optical methane sensor based on insertion of cryptophane-E cavity in 1D photonic crystal," Opt. Mem. Neural Networks **31**, 403–412 (2022).
[79]T. Hong, J. T. Culp, K.-J. Kim, J. Devkota, C. Sun, and P. R. Ohodnicki, "State-of-the-art of methane sensing materials: A review and perspectives," TrAC, Trends Anal. Chem. **125**, 115820 (2020).
[80]X.-D. Wang and O. S. Wolfbeis, "Fiber-optic chemical sensors and biosensors (2008–2012)," Anal. Chem. **85**, 487–508 (2013).
[81]J. Yang, L. Xu, and W. Chen, "An optical fiber methane gas sensing film sensor based on core diameter mismatch," Chin. Opt. Lett. **8**, 482–484 (2010).
[82]M. Benounis, N. Jaffrezic-Renault, J.-P. Dutasta, K. Cherif, and A. Abdelghani, "Study of a new evanescent wave optical fibre sensor for methane detection based on cryptophane molecules," Sens. Actuators, B **107**, 32–39 (2005).
[83]F. N. Kissell, *Handbook for Methane Control in Mining* (Department of Health and Human Services, Centers for Disease Control and Prevention, National Institute for Occupational Safety and Health, 2006).
[84]Y.-n. Zhang, Y. Zhao, and Q. Wang, "Measurement of methane concentration with cryptophane E infiltrated photonic crystal microcavity," Sens. Actuators, B **209**, 431–437 (2015).
[85]H. Liu, C. Chen, Y. Zhang, B. Bai, and S. Tang, "A high-sensitivity methane sensor with localized surface plasmon resonance behavior in an improved hexagonal gold nanoring array," Sensors **19**, 4803 (2019).
[86]W. Xiao, X. Fan, Y. Wang, W. Fang, F. Sun, J. Zhao, X. Wei, C. Li, J. Tao, and S. Kumar, "High-Q fano resonance metasurface sensor for refractive index and methane gas concentration measurement," Opt. Commun. **574**, 131187 (2025).
[87]H. Liu, X. Zhang, B. Zhao, B. Wu, H. Zhang, and S. Tang, "Simultaneous measurements of refractive index and methane concentration through electromagnetic fano resonance coupling in all-dielectric metasurface," Sensors **21**, 3612 (2021).
[88]H. Jiang, B. Wang, and Z. Liu, "New dual-peak high-performance structure utilizing terahertz metamaterial metasurface for concentration detection of H_2 and CH_4 gases," Opt Laser. Technol. **186**, 112728 (2025).
[89]C. Chen, H. Liu, Y. Zhang, B. Bai, and Q. Shao, "High-sensitive gas-mixture detection based on Mie resonance in slotted MDM metasurface," Optik **242**, 167096 (2021).